



Iterative Image Restoration Combining Total Variation Minimization and a Second-Order Functional*

MARIUS LYSAKER

Department of Scientific Computing, Simula Research Laboratory, AS, Norway
 mariul@simula.no

XUE-CHENG TAI

Department of Mathematics, University of Bergen, N-5008, Bergen, Norway, and Institute of Mathematics, Henan University, Kaifeng, 475001, P.R. China
 tai@mi.uib.no

Received January 20, 2004; Revised February 8, 2005; Accepted February 8, 2005

Abstract. A noise removal technique using partial differential equations (PDEs) is proposed here. It combines the Total Variational (TV) filter with a fourth-order PDE filter. The combined technique is able to preserve edges and at the same time avoid the staircase effect in smooth regions. A weighting function is used in an iterative way to combine the solutions of the TV-filter and the fourth-order filter. Numerical experiments confirm that the new method is able to use less restrictive time step than the fourth-order filter. Numerical examples using images with objects consisting of edge, flat and intermediate regions illustrate advantages of the proposed model.

Keywords: iterative image restoration, convex combination, characteristic features, PDEs

1. Introduction

An approach to recover an image u from a noisy observation u_0 is proposed in this work. Digital images can basically be decomposed into three distinguished areas; flat regions, regions with a smooth change in the intensity value, and jumps. The aim of all noise removal algorithms is to restore and enhance these characteristics by filtering out noise. Total Variation (TV) minimization is a successful approach to recover images with sharp edges. This method was proposed by Rudin, Osher and Fatemi (ROF) in Rudin et al. (1992). The TV minimization method finds u where

the following is satisfied

$$\min_u E_1(u), \text{ where } E_1(u) = \int_{\Omega} |\nabla u| \, dx dy + \frac{\lambda_1}{2} \int_{\Omega} |u - u_0|^2 \, dx dy. \quad (1)$$

Here, $\Omega \subset \mathbb{R}^2$ is the domain where the image is defined, $\lambda_1 > 0$ is a parameter that controls contribution of the fidelity term $\int_{\Omega} |u - u_0|^2 \, dx dy$, and $\int_{\Omega} |\nabla u| \, dx dy$ is in fact the total variation of u (see Ziemer (1989) and Giusti (1998) for definitions). When u is not differentiable, $|\nabla u|$ is understood as a measure. More precisely,

$$\int_{\Omega} |\nabla u| \, dx dy = \sup \left\{ \int_{\Omega} u \operatorname{div} v \, dx dy : v \right.$$

*This work has been supported by the Research Council of Norway.

$$= (v_1, v_2) \in C_0^\infty(\Omega), v_1^2(x, y) + v_2^2(x, y) \leq 1 \text{ for } (x, y) \in \Omega \}. \quad (2)$$

See p. 221 of Ziemer (1989) for some more details.) This term is generally called a regularization term and it is used here to penalize oscillations. A superior advantage of the TV-norm regularization is that discontinuities are allowed. However, both from a theoretical (Weickert, 1998; Ring, 2000) and experimental (Lysaker et al., 2003; Chambolle and Lions, 1997; Chan et al., 2000) point of view, it has been shown that the TV-norm transforms smooth signal into piecewise constants, the so-called staircase effect. To overcome this spurious effect, higher-order PDEs have been of special interest over the last few years (Lysaker et al., 2003; Chan et al., 2000; You and Kaveh, 2000; Lysaker et al., 2004; Osher et al., 2003; Bertozzi and Greer, 2004; Greer and Bertozzi, 2003a, 2003b, 2004; Scherzer, 1998; Hinterberger and Scherzer, 2004). The theoretical analysis of Bertozzi and Greer (2003), Bertozzi and Greer (2003), and Scherzer (1998) reveals that fourth-order PDEs enjoy some special properties that are not valid for the second-order PDEs. The higher-order PDEs are generally coming from the minimization of functionals as

$$\min_u \int_{\Omega} F(x_1, x_2, \dots, x_k, u, du, d^2u, \dots, d^k u) \times dx_1 dx_2 \dots dx_k, \quad (3)$$

where $d^k u$ is the partial derivatives of u of order k . For $\Omega \subset \mathbb{R}^n$ and $n \geq 2$, mixed derivative may occur in (3). One of the functionals of focus in this paper was first proposed by Lysaker, Lundervold and Tai (LLT) in a previous work (Lysaker et al., 2003):

$$\begin{aligned} \min_u E_2(u), \text{ where } E_2(u) \\ = \int_{\Omega} (u_{xx}^2 + u_{xy}^2 + u_{yx}^2 + u_{yy}^2)^{\frac{1}{2}} dx dy \\ + \frac{\lambda_2}{2} \int_{\Omega} |u - u_0|^2 dx dy, \end{aligned} \quad (4)$$

where the parameter $\lambda_2 > 0$ balances the regularity of the solution and how well u fits the noisy data u_0 . Minimizing functional (4) yields a nonlinear fourth-order PDE. The details about how to get this nonlinear fourth-order PDE and its boundary conditions were omitted in Lysaker et al. (2003) due to its complexity.

In this work, we shall supply these details together with some details about its numerical implementations.

Higher-order PDEs are known to recover smoother surfaces. Dealing with higher-order PDEs a major challenge is to pursue the quality of (1) along jumps. Unfortunately, it seems to be a hard case to get one method to preserve discontinuities in one part of the image and simultaneously recover smooth signals in other parts. Hence, a combination of different methods may be needed to improve the image restoration capability. Our approach is to involve both a lower- and a higher-order PDE, a solution strategy motivated by (Chambolle and Lions, 1997; Chan et al., 2000; Karkkainen and Majava, 2000; Ito and Kunisch, 2000), among others.

The novelty in this work is to involve the restoration properties of (1) together with (4), i.e. using convex combination of the solutions of (1) and (4). By analyzing underlying features or the local trend in the image of interest, we can combine (1) and (4) in such a way that both smooth and discontinuous signals are handled properly. The ROF (Rudin, 1992) model (1) is known to be better than the LLT (Lysaker et al., 2003) model (4) when identifying locations of discontinuities and the amplitude of jumps. The LLT model handles smooth signals better than the ROF model. A combined model is able to utilize the best properties of each of the two models, and manage to overcome the weaknesses of both.

Different approaches for adaptive image restoration methods have been considered before (Chambolle and Lions, 1997; Chan et al., 2000; Karkkainen and Majava, 2000; Ito and Kunisch, 2000; Nagao and Matsuyama, 1979; Terzopoulos, 1986; Terzopoulos, 1988). In Chambolle and Lions (1997), u was decomposed into a sum of a smooth function u_1 and a function u_2 that contained the jumps. They solved an inf-convolution problem concerning u_1 and u_2 . The strategy in Chan et al., (2000) was to introduce an elliptic operator together with (1). This substantially reduced the staircase effect, while edges were preserved. Further, in Karkkainen and Majava (2000), functional (1) was modified by the extra term $\frac{\mu}{2} \int_{\Omega} |\nabla u|^2 dx dy$, $\mu > 0$. This ensures convexity of the cost functional in $H_0^1(\Omega)$, and yields the unique solvability of the problem in this space. Common drawbacks of the adaptive formulations mentioned above, are the increased number of unknown to determine leading to increased computing time. In Ito and Kunisch (2000) they employed and

generalized the enhancement technique based on BV- and Perona-Malik-type regularization methods. A cost functional consisting of a data fitting term and a restoration energy criterion for objects consisting of edge, flat, and intermediate regions was minimized. Global convergence was proven.

The idea we use here seems to have some similarities with the ideas used in Nagao and Matsuyama (1979) and Terzopoulos (1986, 1988). For example, the following functional is used as a regularization term in Terzopoulos (1988) in computing a visible-surface representation $u(x, y)$;

$$S_{\rho\tau}(u) = \frac{1}{2} \int_{\Omega} \rho(x, y) \{ \tau(x, y) (u_{xx}^2 + 2u_{xy}^2 + u_{yy}^2) + [1 - \tau(x, y)] (u_x^2 + u_y^2) \} dx dy.$$

The function $\rho(x, y)$ is chosen to be small at jumps and $\tau(x, y) \in [0, 1]$ is used to control the regularity of the surface. In our approach, ρ is not necessary due to the use of the total variational norms and the function of τ is replaced by a linear combination technique using a weighting function. The approach using the weighting function could automatically detect jumps and smooth regions. Thus, it has better properties and is easy and cheap to compute.

To deal with the unknown parameters presented in our approach, i.e. λ_1 in (1) and λ_2 in (4), we assume the noise level

$$\sigma^2 = \int_{\Omega} |u - u_0|^2 dx dy \quad (5)$$

to be approximately known. The minimizers for (1) and (4) can then be combined with (5) to find an optimal value for λ_1 and λ_2 , respectively. Without this assumption, λ_1 and λ_2 can be found by trial and error, or by adjusting a parameter $\bar{\sigma}$ to approximate the true noise level σ in (5). Examples of image restoration with such approximation of the noise level will also be evaluated.

Section 2 of this paper gives a detailed description of minimization problem (4), and we formally introduce the fourth-order PDE appearing in the image restoration model. This fourth-order PDE together with a second-order PDE are the basic ingredients in our composed model. The way these two PDEs interfere with each other is discussed in Section 3. Implementation details are given in Section 4. Section 5 is devoted to numerical examples, followed by some conclusions in Section 6.

2. Description of Minimization Problem (4)

It is in our interest to restore an image that is contaminated with noise. We use functionals E_i , $i = 1, 2$, to measure the quality of the restoration process. Smaller values of E_i correspond to a result that reflects features (flat, smooth and jumps) in a better way than larger values do. One of the two basis functionals in our approach is given by (1). From Rudin et al. (1992) we know that minimizing functional (1) yields the associated Lagrange equation

$$-\nabla \cdot \left(\frac{\nabla u}{|\nabla u|} \right) + \lambda_1 (u - u_0) = 0 \text{ in } \Omega, \quad \frac{\partial u}{\partial n} = 0 \text{ on } \partial\Omega. \quad (6)$$

Further, recall from Rudin et al. (1992) that the unknown parameter λ_1 is given by

$$\lambda_1 = -\frac{1}{\sigma^2} \int_{\Omega} \left(\frac{\nabla u}{|\nabla u|} \right) \cdot \nabla (u - u_0) dx dy. \quad (7)$$

An iterative method is used to solve (6) and (7) so that the solution satisfies these equations at steady state, c.f. Rudin et al. (1992). We want to find an equivalent formulation for minimization problem (4). For simplicity we introduce the notation $|D^2 u| = (\nabla u_x \cdot \nabla u_x + \nabla u_y \cdot \nabla u_y)^{\frac{1}{2}} = (u_{xx}^2 + u_{xy}^2 + u_{yx}^2 + u_{yy}^2)^{\frac{1}{2}}$ and write

$$E_2(u) = \int_{\Omega} |D^2 u| dx dy + \frac{\lambda_2}{2} \int_{\Omega} |u - u_0|^2 dx dy. \quad (8)$$

To find a weak solution for (8) we must investigate

$$\frac{\partial E}{\partial u} \cdot v = \int_{\Omega} \left(\frac{\nabla u_x \cdot \nabla v_x + \nabla u_y \cdot \nabla v_y}{|D^2 u|} \right) dx dy + \lambda_2 \int_{\Omega} (u - u_0) v dx dy = 0. \quad (9)$$

Using Green's lemma on the first part of (9) we get

$$\begin{aligned} & \int_{\Omega} \left(\frac{\nabla u_x \cdot \nabla v_x + \nabla u_y \cdot \nabla v_y}{|D^2 u|} \right) dx dy \\ &= \int_{\partial\Omega} \left(\frac{1}{|D^2 u|} \frac{\partial u_x}{\partial n} \right) v_x + \left(\frac{1}{|D^2 u|} \frac{\partial u_y}{\partial n} \right) v_y dS \\ & \quad - \int_{\Omega} \nabla \cdot \left(\frac{\nabla u_x}{|D^2 u|} \right) v_x + \nabla \cdot \left(\frac{\nabla u_y}{|D^2 u|} \right) v_y dx dy, \end{aligned} \quad (10)$$

where dS denotes the surface measure on $\partial\Omega$. Here and later, the unit normal vector on $\partial\Omega$ is denoted by $n = (n_1, n_2)$. Let us also introduce the notation $\bar{G} = [g_1, g_2] = [\nabla \cdot (\frac{\nabla u_x}{|D^2u|}), \nabla \cdot (\frac{\nabla u_y}{|D^2u|})]$. Applying Green's lemma on the vector field \bar{G} , we obtain

$$\begin{aligned} & \int_{\Omega} \bar{G} \cdot \nabla v \, dx dy \\ &= \int_{\partial\Omega} \bar{G} \cdot n \, v \, dS - \int_{\Omega} \nabla \cdot \bar{G} \, v \, dx dy. \end{aligned} \quad (11)$$

By combining (10) and (11) together with the notation of \bar{G} , we see that

$$\begin{aligned} & \int_{\Omega} \left(\frac{\nabla u_x \cdot \nabla v_x + \nabla u_y \cdot \nabla v_y}{|D^2u|} \right) dx dy \\ &= \int_{\partial\Omega} \left(\frac{1}{|D^2u|} \frac{\partial u_x}{\partial n} \right) v_x + \left(\frac{1}{|D^2u|} \frac{\partial u_y}{\partial n} \right) v_y \, dS \\ &\quad - \int_{\partial\Omega} \nabla \cdot \left(\frac{\nabla u_x}{|D^2u|} \right) n_1 \, v + \nabla \cdot \left(\frac{\nabla u_y}{|D^2u|} \right) n_2 \, v \, dS \\ &\quad + \int_{\Omega} \left(\nabla \cdot \left(\frac{\nabla u_x}{|D^2u|} \right) \right)_x v \\ &\quad + \left(\nabla \cdot \left(\frac{\nabla u_y}{|D^2u|} \right) \right)_y v \, dx dy. \end{aligned} \quad (12)$$

From this we conclude that a minimum for (8) occurs when

$$\begin{aligned} & \left(\frac{u_{xx}}{|D^2u|} \right)_{xx} + \left(\frac{u_{xy}}{|D^2u|} \right)_{yx} + \left(\frac{u_{yx}}{|D^2u|} \right)_{xy} \\ & \quad + \left(\frac{u_{yy}}{|D^2u|} \right)_{yy} + \lambda_2(u - u_0) = 0. \end{aligned} \quad (13)$$

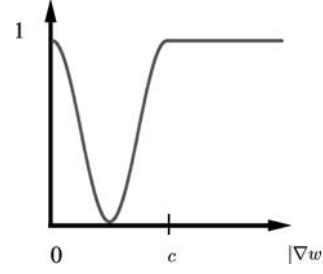


Figure 1. An example of the weight function Θ given by (19).

If Ω is a rectangular domain, with an outer normal $n = (n_1, n_2)$, we see from (12) that the variational equality (9) implies the following the boundary conditions

$$\left. \begin{aligned} u_{xx} + u_{yx} &= 0 \\ \left(\frac{u_{xx}}{|D^2u|} \right)_x + \left(\frac{u_{xy}}{|D^2u|} \right)_y &= 0 \end{aligned} \right\} \quad (14)$$

on $\partial\Omega$ where n is orthogonal to the y -axis,

$$\left. \begin{aligned} u_{yy} + u_{xy} &= 0 \\ \left(\frac{u_{yx}}{|D^2u|} \right)_x + \left(\frac{u_{yy}}{|D^2u|} \right)_y &= 0 \end{aligned} \right\} \quad (15)$$

on $\partial\Omega$ where n is orthogonal to the x -axis.

The value of λ_2 also needs to be determined such that (13) has a steady state with condition (5) fulfilled at the steady state. We use the same idea as in Rudin et al. (1992) to obtain such a formula for λ_2 . We simply multiply (13) by $u - u_0$, integrate over Ω , and make

Table 1. Discretization used in the implementations.

$D_x^\pm(u_{i,j})$	$\pm \frac{1}{\Delta x} [u_{i\pm 1,j} - u_{i,j}]$
$D_y^\pm(u_{i,j})$	$\pm \frac{1}{\Delta y} [u_{i,j\pm 1} - u_{i,j}]$
$D_{xx}(u_{i,j})$	$\frac{1}{\Delta x} [D_x^+(u_{i,j}) - D_x^+(u_{i-1,j})]$
$D_{xy}^\pm(u_{i,j})$	$\pm \frac{1}{\Delta y} [D_x^\pm(u_{i,j\pm 1}) - D_x^\pm(u_{i,j})]$
$D_{yx}^\pm(u_{i,j})$	$\pm \frac{1}{\Delta x} [D_y^\pm(u_{i\pm 1,j}) - D_y^\pm(u_{i,j})]$
$D_{yy}(u_{i,j})$	$\frac{1}{\Delta y} [D_y^+(u_{i,j}) - D_y^+(u_{i,j-1})]$
$ D_x(u_{i,j}) $	$\sqrt{(D_x^+(u_{i,j}))^2 + (m[D_y^+(u_{i,j}), D_y^-(u_{i,j})])^2} + \epsilon$
$ D_y(u_{i,j}) $	$\sqrt{(m[D_x^+(u_{i,j}), D_x^-(u_{i,j})])^2 + (D_y^+(u_{i,j}))^2} + \epsilon$
$ D^2(u_{i,j}) $	$\sqrt{(D_{xx}(u_{i,j}))^2 + (D_{xy}^+(u_{i,j}))^2 + (D_{yx}^+(u_{i,j}))^2 + (D_{yy}(u_{i,j}))^2} + \epsilon$

use of (5) to get

$$\lambda_2 = \frac{-1}{\sigma^2} \int_{\Omega} \left(\frac{u_{xx}}{|D^2u|} (u - u_0)_{xx} + \frac{u_{xy}}{|D^2u|} (u - u_0)_{yx} + \frac{u_{yx}}{|D^2u|} (u - u_0)_{xy} + \frac{u_{yy}}{|D^2u|} (u - u_0)_{yy} \right) dx dy. \quad (16)$$

In this section we have treated $E_1(u)$ and $E_2(u)$ and their associated Lagrangian equations separately. However, we want to establish a positive interaction between these equations and that is the topic for the next section.

3. Convex Combination of the Two Minimization Problems

Here, we use the notation u and v to distinguish the solutions of (6) and (13) respectively. From the Euler-Lagrange variational principle, the minimizer of u and the minimizer of v can be interpreted as the steady state solution of the nonlinear diffusion process

$$u_t = \nabla \cdot \left(\frac{\nabla u}{|\nabla u|} \right) - \lambda_1 (u - u_0), \quad \text{and} \quad (17)$$

$$v_t = - \left(\frac{v_{xx}}{|D^2v|} \right)_{xx} - \left(\frac{v_{xy}}{|D^2v|} \right)_{yx} - \left(\frac{v_{yx}}{|D^2v|} \right)_{xy} - \left(\frac{v_{yy}}{|D^2v|} \right)_{yy} - \lambda_2 (v - u_0), \quad (18)$$

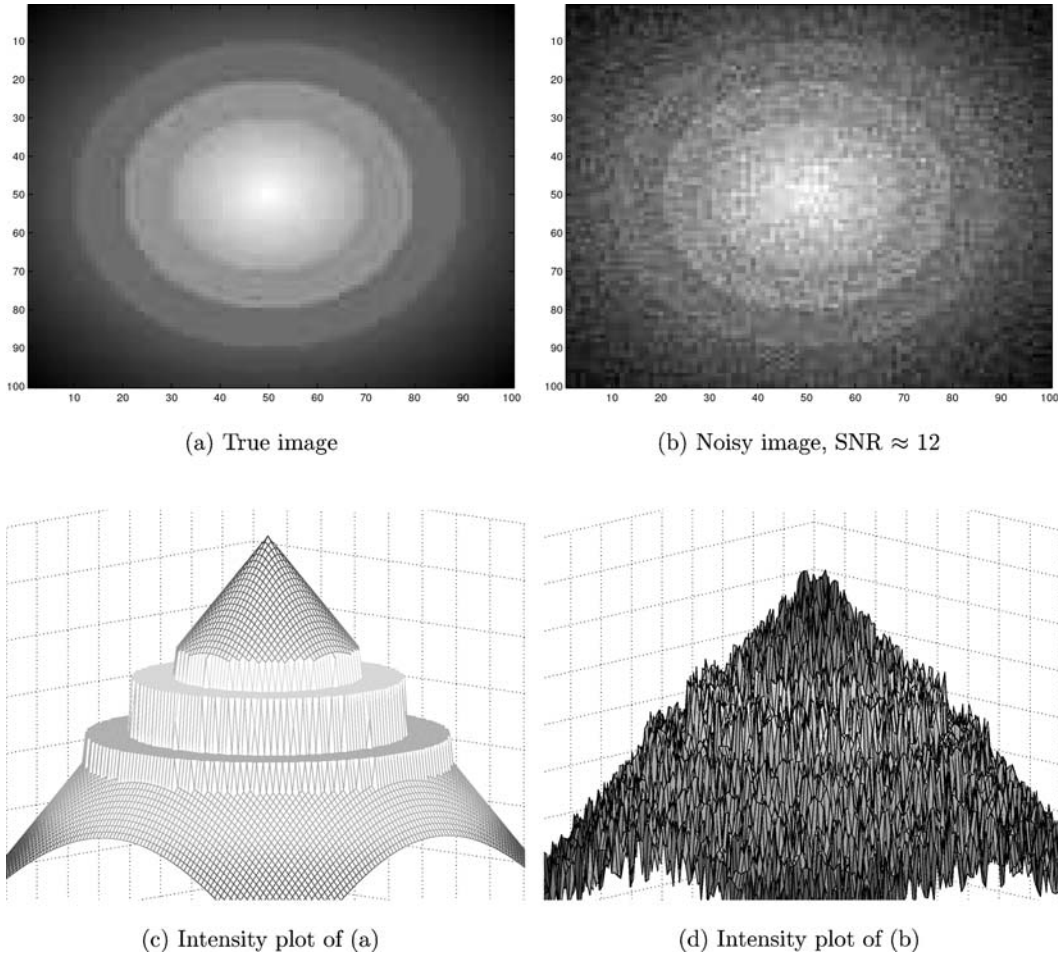


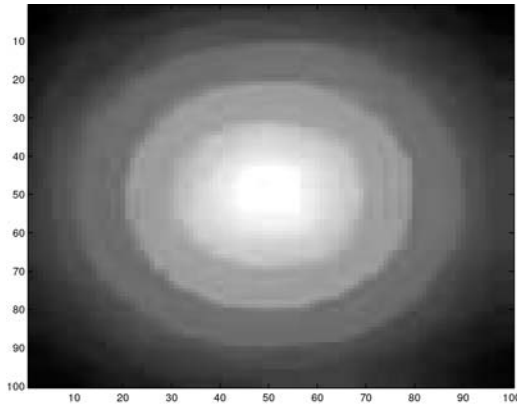
Figure 2. Two different ways to visualize the same data are given in the upper and lower column. Regions with high function values in the lower column correspond to bright regions in the images at the upper column.

where we respectively use the initial condition $u(x, y, 0) = u_0(x, y)$ and $v(x, y, 0) = u_0(x, y)$. Each of the above PDEs substantially suppress noise, but we do not expect their solutions u and v to be equal all over the image domain Ω , mainly because (17) does not penalize discontinuities while (18) is known to recover smoother surfaces. Both methods have their strengths and weaknesses depending on the characteristics of the image of interest. Because of this, we want to generate a new solution by taking the best from each of the two methods by a convex combination $w = \theta u + (1-\theta)v$, for $\theta \in [0, 1]$. We prefer that the weighting function θ be found adaptively. Due to the strengths and weaknesses of the two models, it is desirable that the weighting function $\theta = 1$ along edges and in flat regions, emphasizing the restoration properties for (17). To emphasize the restoration properties for (18) in smooth regions we

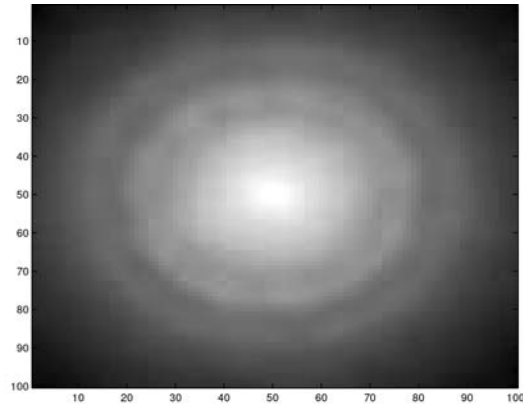
want $0 \leq \theta < 1$. By testing several different approaches calculating the weighting function, we have found the procedure to update θ discussed below is rather stable and gives good results.

Assume that we have a weighting function θ^{old} , a function u which is an intermediate solution of (17) and a function v which is an intermediate solution of (18). We shall find a new weighting function θ^{new} according to

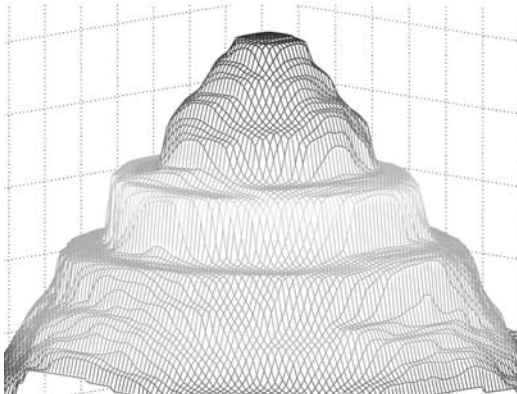
$$\theta^{\text{new}} = \begin{cases} 1 & \text{if } |\nabla w| \geq c \\ \frac{1}{2} \cos\left(\frac{2\pi|\nabla w|}{c}\right) + \frac{1}{2} & \text{elsewhere,} \end{cases} \quad (19)$$



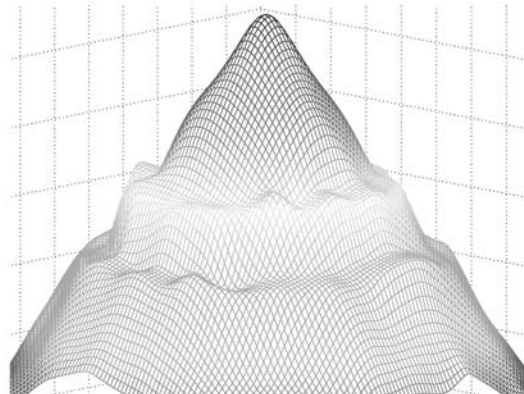
(a) Processed with ROF



(b) Processed with LLT



(c) Intensity plot of (a)



(d) Intensity plot of (b)

Figure 3. Two different approaches are used to find an improved image from the noisy image given in Fig. 3(b). Only the central portion of the intensity plots is depicted in the lower column.

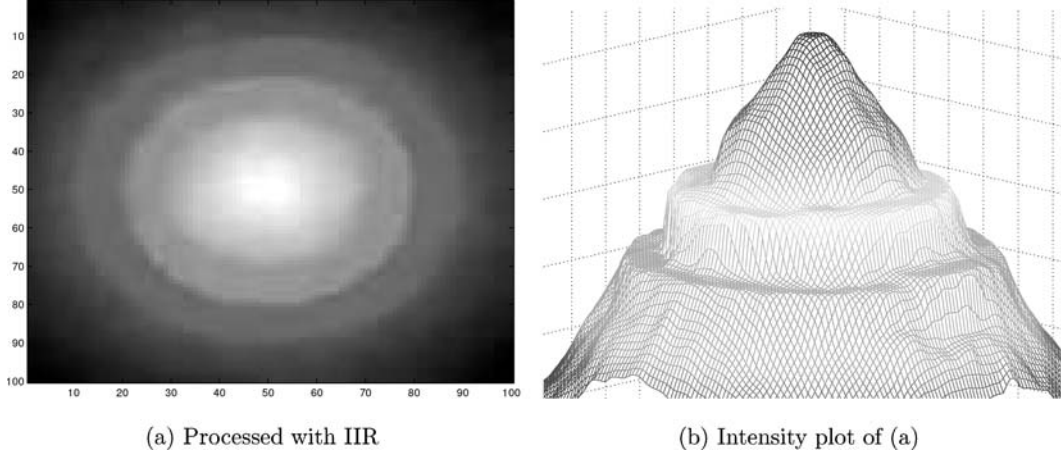


Figure 4. IIR is used to find an improved image from the noisy image given in Fig. 2(b). Only the central portion of the intensity plot is depicted here.

where $w = \theta^{\text{old}}u + (1 - \theta^{\text{old}})v$. We define this mapping from $u, v, \theta^{\text{old}}$ to θ^{new} as ψ , i.e. $\theta^{\text{new}} = \psi(\theta^{\text{old}}, u, w)$. For large and small values of $|\nabla w|$ the weight θ approaches 1, and for intermediate values of $|\nabla w|$ the weight function is closer to 0. The positive parameter c must be adjusted so that θ reaches its minimum value in regions that are linearly sloped. A typical example of the relationship between $|\nabla w|$, c and θ are given in Fig. 1.

Choosing $0 \ll c < 1$ means that only the absolute largest jumps are unaffected of the fourth-order PDE (18). Since only small jumps (staircase effect) caused by (17) should be suppressed with fourth-order PDE (18) we found $c \in (\frac{1}{20}, \frac{1}{5})$ to be a proper value if $|\nabla w|$ is scaled to take values in the interval $[0, 1]$. With this choice of c intermediate jumps were protected while the staircase effect was suppressed, but this parameter is image dependent.

4. Implementation Details

To discretize Eqs. (17) and (18), we use finite differences. Let Δx and Δy be the mesh sizes for the x and y variables, and Δt be the time step. We denote by u^k

Table 2. SNR, L^2 -norm and Δt_{max} for the different schemes.

Method	SNR	L^2 -norm	Δt_{max} (CFL)
ROF	115	$1.64 \cdot 10^4$	0.35
LLT	148	$1.66 \cdot 10^4$	0.09
IIR	163	$1.22 \cdot 10^4$	0.17

and v^k the approximations for $u(x, y, k \Delta t)$ and $v(x, y, k \Delta t)$ respectively, where x and y are the grid points. The approximations we have used in our scheme is outlined in Table 1.

To simplify the notations, we will omit the subscripts i, j and use u^k to denote $u_{i,j}^k$. In Table 1 we have used the notation $m[a, b] = (\frac{\text{sign } a + \text{sign } b}{2}) \min(|a|, |b|)$. The details of the algorithm we have used are given in the following.

Algorithm 1.

Given $\theta^0 \in [0, 1]$, $c \in [0, 1]$ and put $u^0 = v^0 = u_0$. For $k = 0, 1, \dots, d$

1. Find λ_1^k by (7) and update

$$\begin{aligned} \tilde{u}^{k+1} = & u^k + \Delta t D_x^- \left(\frac{D_x^+ u^k}{|D_x u^k|} \right) \\ & + \Delta t D_y^- \left(\frac{D_y^+ u^k}{|D_y u^k|} \right) - \Delta t \lambda_1^k (u^k - u_0). \end{aligned} \quad (20)$$

2. Find λ_2^k by (16) and update

$$\begin{aligned} \tilde{v}^{k+1} = & v^k - \Delta t \left[D_{xx} \left(\frac{D_{xx} v^k}{|D^2 v^k|} \right) + D_{yx}^- \left(\frac{D_{xy}^+ v^k}{|D^2 v^k|} \right) \right. \\ & \left. + D_{xy}^+ \left(\frac{D_{yx}^- v^k}{|D^2 v^k|} \right) + D_{yy} \left(\frac{D_{yy} v^k}{|D^2 v^k|} \right) \right] \\ & - \Delta t \lambda_2^k (v^k - u_0). \end{aligned} \quad (21)$$

3. Find θ^{k+1} from (19), i.e.

$$\theta^{k+1} = \psi(\theta^k, \tilde{u}^{k+1}, \tilde{v}^{k+1}).$$

4. Do the convex combination

$$u^{k+1} = \theta^{k+1} \tilde{u}^{k+1} + (1 - \theta^{k+1}) \tilde{v}^{k+1}, \text{ and let } v^{k+1} = u^{k+1}.$$

When evaluating the finite differences for (20) and (21), the boundary conditions (6) and (14)–(15) are needed. Implementation of (6) is explained in Rudin et al. (1992), and implementation of (14)–(15) follows from Table 1.

Notice that a convex combination is done in each iteration for this algorithm. Another approach could be to find the solution u and v independent of each other, and combine them at convergence. Numerical tests indicate that a combination in each iteration is most effective and accurate. Each of the numerical schemes (20) and (21) are stable if they are solved separately, as long as Δt fulfills the Courant-Friedrichs-Lewy (or CFL) stability criterion. Numerical tests have shown that the same holds if we combine them in each iteration. Moreover, the time step needed by the combined scheme Algorithm 1 is always larger than in the fourth-order scheme; the combined scheme not only improves the quality of the processed image; it also improves the efficiency compared with the fourth-order scheme.

Table 3. SNR, L^2 -norm and Δt_{\max} for the different schemes.

Method	SNR	L^2 -norm	Δt_{\max} (CFL)
ROF	35	$4.79 \cdot 10^6$	1.10
LLT	40	$4.26 \cdot 10^6$	0.24
IIR	43	$4.05 \cdot 10^6$	0.80

5. Numerical results

In this section we present some of the results obtained with the proposed Iterative Image Restoration (IIR) model by alternating between PDE (17) and PDE (18). Our results will be compared with the standard ROF model (Rudin et al., 1992) given by solving PDE (17), and the LLT model Lysaker et al. (2003) given by solving PDE (18). For the numerical examples we will use images composed of flat subregions, subregions with a smooth change in the intensity value, and jumps. We expect ROF to restore and enhance jumps more precisely than LLT does. On the other hand, we expect LLT to process smooth subregions more correctly than ROF does. See Lysaker et al. (2003) for a closer evaluation of ROF and LLT. Using IIR the aim is to take the best out of each of these methods to recover both jumps and smooth signals accurately.

In Fig. 2, two gray-level images are depicted, together with the corresponding intensity plots. At first

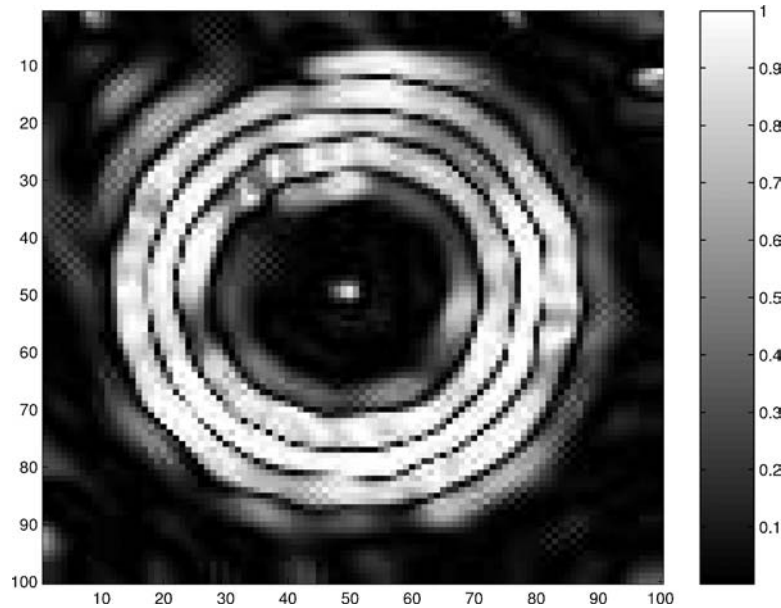


Figure 5. Weight function θ at convergence.

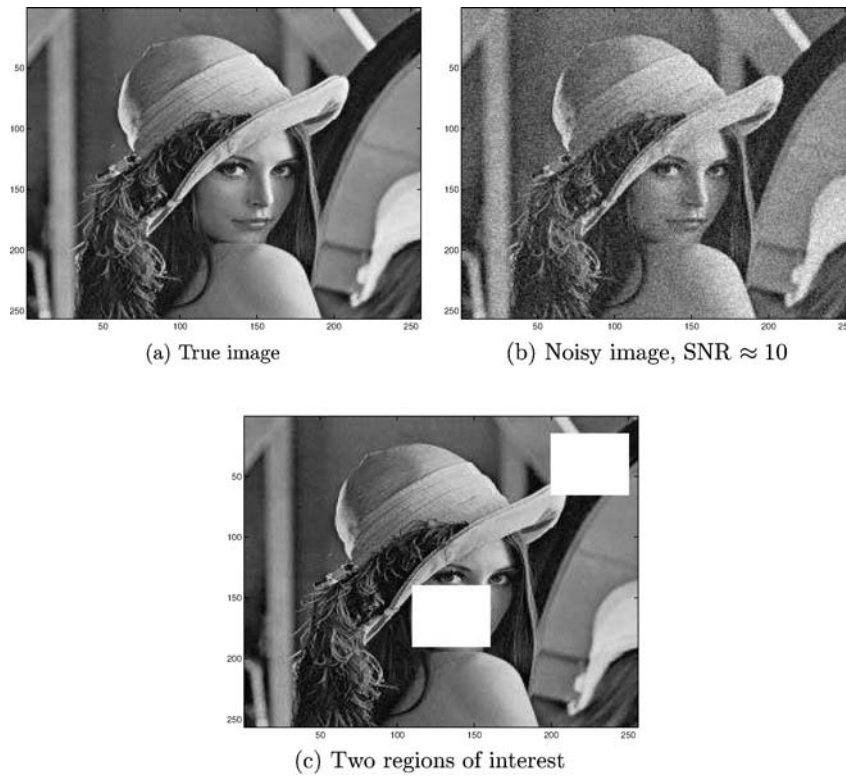


Figure 6. Lena image corrupted with Gaussian distributed noise. The white rectangles in (c) indicate two regions of special interest, i.e. one typical smooth region and one region with discontinuities.

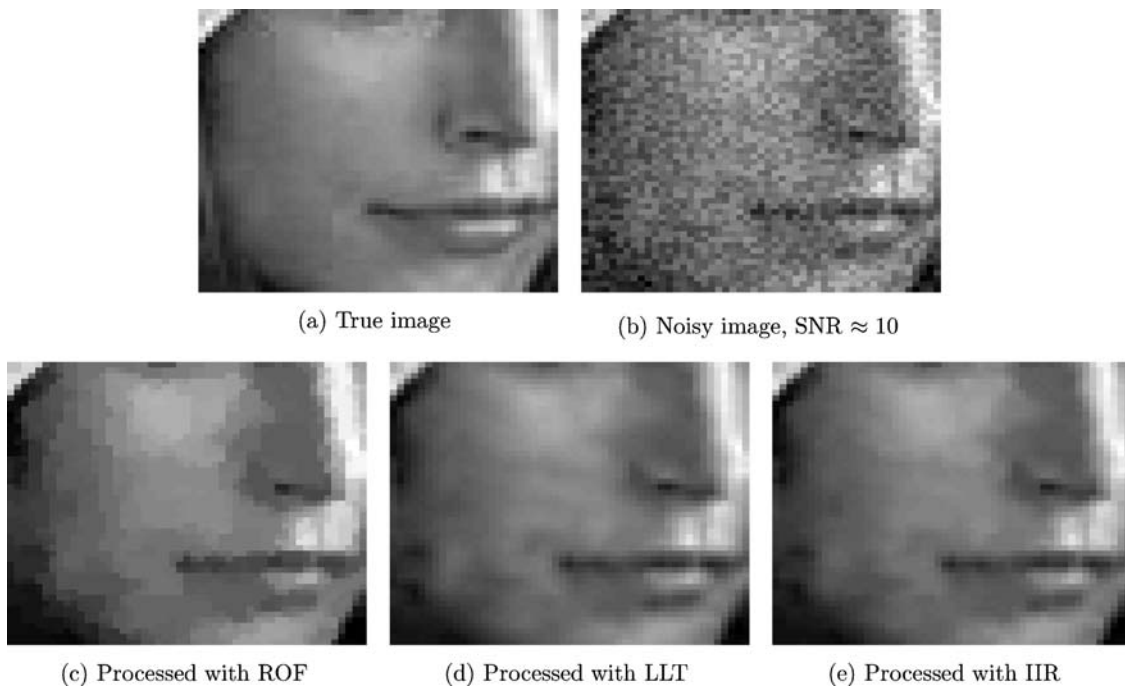


Figure 7. A small portion of the Lena image is shown to better emphasize disparities in the smooth surface.

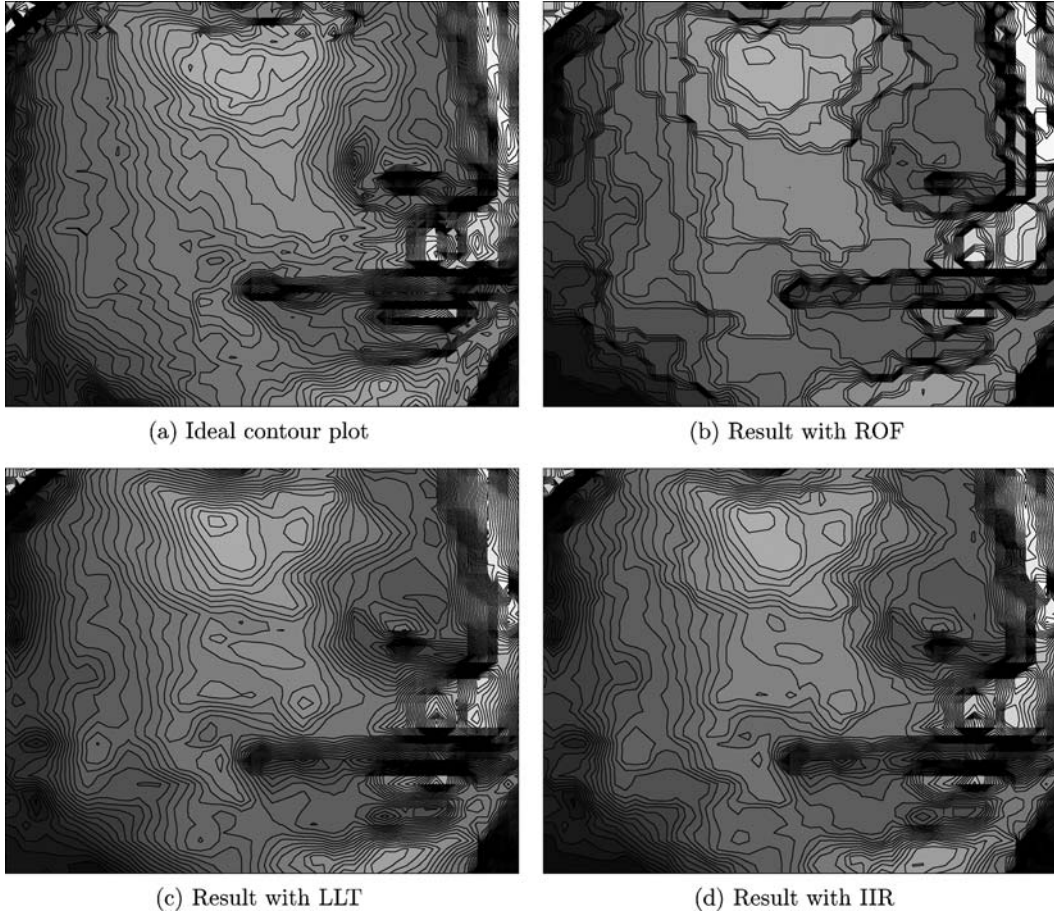


Figure 8. A small portion of the Lena image is visualized with a contour plot to better emphasize disparities between the models.

glance, one may mistakenly think that the bright region in the central part of the image in Fig. 2(a) takes a constant intensity value, but the intensity plot in Fig. 2(c) reveals that there is a smooth change in the intensity value in this region. To emphasize these details it is therefore essential to visualize the results with both intensity plots and contour plots when we compare the performance for the different schemes. To do a thorough evaluation, we will also investigate and report the signal-to-noise-ratio (SNR) and the L_2 -norm of the difference between the recovered image and the true image. For a given image u and its noise observation u_0 , the noise is denoted as $\eta = u_0 - u$. The following formula has been used to calculate the SNR for the numerical experiments for a given image u and noise η ;

$$\text{SNR} = \frac{\int_{\Omega} (u_0 - \bar{u}_0)^2 dx dy}{\int_{\Omega} (\eta - \bar{\eta})^2 dx dy},$$

$$\text{where } \bar{u}_0 = \frac{1}{|\Omega|} \int_{\Omega} u_0 dx dy, \text{ and}$$

$$\bar{\eta} = \frac{1}{|\Omega|} \int_{\Omega} \eta dx dy.$$

In our first example, we used the noisy data shown in Fig. 2(b) as input to the ROF, LLT and IIR. Before processing, we observed $\|u_0 - u_{\text{true}}\|_{L_2}^2 \approx 1.88 \cdot 10^5$ and $\text{SNR} \approx 12$. There are several reasons for examine the image shown in Fig. 2(a). First of all, it consists of a rotationally invariant object, i.e. circular edges. Secondly, evaluating an object like this should provoke the strengths and the weaknesses for the three restoration methods listed above.

In this first test we were specially interested in evaluating (i) the ability to reproduce the cone on the top of the object, (ii) the ability to maintain the height of the object, (iii) the ability to reproduce jumps and flat

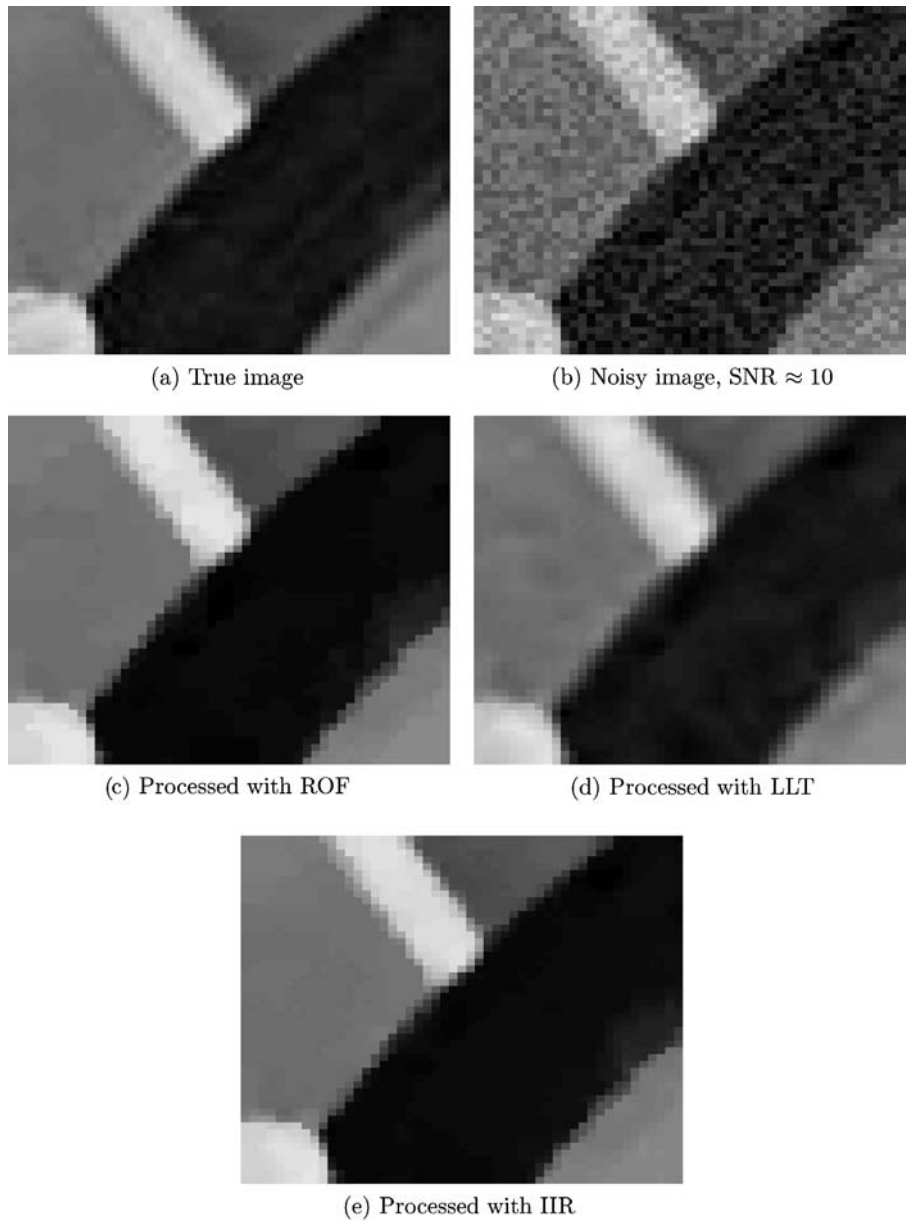


Figure 9. A part of the Lena image with discontinuities.

regions, and (iv) the spurious staircase effect in smooth regions.

Let us first focus on the result obtained with ROF depicted in Fig. 3(a) and (c). The smooth change in the intensity value (i.e. the cone) is recovered as piecewise constant subregions, as seen in Fig. 3(c). This is a known byproduct of the TV-norm methods in image restoration. On the other hand, flat regions and all edges in this image are recovered accurate by ROF. Concern-

ing the result obtained with LLT, we observe that the staircase effect in smooth regions is suppressed but edges are not recovered that accurately with this model. By comparing Fig. 3(c)–(d) with Fig. 2(c), the strengths and the weaknesses of the restoration schemes ROF and LLT are clearly visible.

All edges are recovered accurately with the iterative model as seen in Fig. 4. At the same time, the staircase effect in smooth regions is avoided. These are

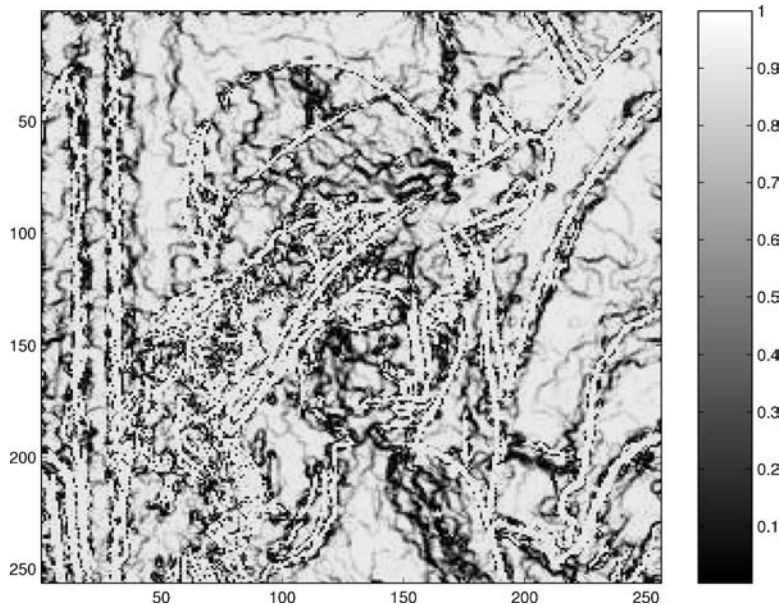


Figure 10. Weight function θ at convergence.

important improvements. Also when we evaluated the SNR and the L^2 -norm some progress was found in the result achieved with the IIR model.

From Table 2 we see that the L^2 -norm is reduced approximately 11.5 times by both ROF and LLT, and 15.5 times by using the IIR model. These numbers indicate that some progress is made with IIR, but the important issues are that IIR recovers smoother sub-surfaces where ROF suffers from the staircase effect and simultaneously preserves discontinuities in other parts of the image. We observed that choosing $\Delta t > \Delta t_{\max}$ made the schemes unstable. The ratio between the three CFL-conditions is representative for what we found in other tests. Higher-order PDEs are known to have more restricted time step than lower-order PDEs. One important observation is that the time step restriction Δt_{\max} for IIR is not bounded by the time step restriction for LLT, although the LLT model is incorporated in the IIR model.

For the convex combination $\theta u + (1 - \theta)v$ in IIR, it is essential that the contributions from v are suppressed at major discontinuities. The weight function θ given by (19) controls the interplay between u from (17) and v from (18) in IIR. In Fig. 5 we visualize θ at convergence. This gray-level image indicates the ratio between (17) and (18) for IIR. It is interesting to observe that all flat regions are marked as bright regions, i.e. $\theta \approx 1$, meaning that no contribution from v occurs in this region. For regions where smooth sub surfaces

should be restored we find $\theta < 1$. This indicates that θ is estimated in accordance with the image features given in Fig. 2(c).

In the next example the Lena image was corrupted with Gaussian distributed noise. Before processing SNR ≈ 10 and L^2 -norm $\approx 1.97 \cdot 10^7$. In real applications the exact noise level is seldom known. To simulate such a case the value we use for σ in (7) and (16) is not the true noise level, but an approximation of the true noise level σ . Let $\bar{\sigma}$ denote the noise level we use for the algorithms and σ denote the true noise level. For the Lena image given in Fig. 6(b) we challenge the schemes by a poor estimate for the amount of noise when we deal with the noise constraint, $\sigma^2 = \frac{10}{14}\bar{\sigma}^2$.

Both ROF, LLT and IIR improve the restoration capacity when the correct estimate for the amount of noise is used for the noise level constraint, but these results are not reported here. As in Table 2, we observe some progress using IIR compared with the two other schemes. However, the important issue is whether IIR recovers smoother sub surfaces where ROF suffers from the staircase effect, and simultaneously preserves discontinuities in other parts, also for natural images. We zoom in the two regions marked with white rectangles in Fig. 6(c) for a more definite evaluation of the processed images.

A small portion of the Lena image is shown in Fig. 7. As expected, ROF transforms smooth subregions like the cheek into piecewise constant regions. Both LLT

and IIR restore images with smoother surfaces that match Fig. 7(a) in a better way. It is not easy to distinguish between the two images depicted in Fig. 7(d) and (e). In this part of the image the weight function θ , given in Fig. 10, emphasize the effect of (18) in the convex combination between (17) and (18) for IIR, and therefore the results from LLT and IIR are similar in this part of the image. This effect is even better visualized in a contour plot given in Fig. 8. From the contours, we see that the results produced by LLT and IIR is much smoother than the result of ROF and they also match the true contours in a better way. All the three methods are able to preserve the discontinuity around the lips and nose.

Next, we want to evaluate the performance of the three different methods in regions that are dominated by discontinuities and piecewise constant signals, see Fig. 9. In regions with edges we observe that ROF restores and enhances these image features in a better way than LLT, (see Fig. 9(c) and (d)). Both ROF and IIR recover images with edges in accordance with Fig. 9(a). It is not easy to distinguish between the two images depicted in Fig. 9(c) and (e). Along the discontinuities the weight function θ , given in Fig. 10, emphasizes the effect of (17) in the convex combination between (17) and (18) for IIR, therefore the results from ROF and IIR are similar in this part of the image.

The weight function θ given by (19) at convergence is shown in Fig. 10. The gray-level indicates the ratio between (17) and (18) for IIR. It is interesting to observe that all major edges are marked as bright regions, i.e. $\theta = 1$, meaning that IIR automatically preserves image boundaries in these regions while suppressing noise.

6. Conclusions

This paper describes a method for filtering gray-scale images corrupted by i.i.d. Gaussian noise. The proposed method combines the TV-norm filter of Rudin, Osher and Fatemi (ROF) in Rudin et al. (1992) with a fourth-order PDE filter of Lysaker, Lundervold and Tai (LLT) in Lysaker et al. (2003). The algorithm, which we call an ‘‘Iterative Image Restoration’’ (IIR) model, is based on a convex combination of the two corresponding solutions of ROF and LLT, and an iterative way to determine the weighted average of these two solutions. We have tested the IIR algorithm on images consisting of edge, flat and smooth sub-regions. The proposed algorithm is able to locate discontinuities as

accurate as the ROF algorithm, and, at the same time do a better job in regions with a smooth variation. Moreover, the combined algorithm is able to use a much less restrictive CFL condition than the fourth-order scheme of LLT. This is confirmed by numerical experiments. Due to the complexity of the equations involved, it is not easy to supply a theoretical verification for this.

References

- Bertozi, A.L. and Greer, J.B. 2003. Low curvature image simplifiers: Global regularity of smooth solutions and laplacian limiting schemes. Tech. rep. (03–26), UCLA, Applied mathematics.
- Chambolle, A. and Lions, P.-L. 1997. Image recovery via total variation minimization and related problems. *Numerische Mathematik*, 76:167–188.
- Chan, T., Marquina, A., and Mulet, P. 2000. High-order total variation-based image restoration. *SIAM Journal on Scientific Computation*, 22:503–516.
- Giusti, E. 1998. *Minimal Surface and Functions of Bounded Variations*. Boston, Birkhäuser.
- Greer, J.B. and Bertozi, A.L. 2004. H^1 solutions of a class of fourth order nonlinear equations for image processing. *Discrete and continuous dynamical systems 2004, special issue in honor of Mark Vishik, Editors: V. Chepyzhov, M. Efendiev, Alain Miramville and Roger Temam*, 1–2(10): 349–366.
- Greer, J.B. and Bertozi, A.L. 2003. Traveling wave solutions of fourth order pdes for image processing. Tech. rep. (03–25), UCLA, Applied mathematics.
- Hinterberger, W. and Scherzer, O. 2004. Variational methods on the space of functions of bounded Hessian for convexification and denoising Preprint.
- Ito, K. and Kunisch, K. 2000. BV-type regularization methods for convoluted objects with edge, flat and grey scales. *Inverse Problems*, 16:909–928.
- Karkkainen, T. and Majava, K. 2000. SAC-methods for image restoration. In *World Scientific and Engineering Society, Greece*, pp. 162–167.
- Lysaker, M., Lundervold, A., and Tai, X.-C. 2003. Noise removal using fourth-order partial differential equation with applications to medical magnetic resonance images in space and time. *IEEE Trans. Image Processing*, 12(12):1579–1590.
- Lysaker, M., Osher, S., and Tai, X.-C. 2004. Noise removal using smoothed normals and surface fitting. *IEEE Trans. Image Processing*, 13(10):1345–1357.
- Nagao, M. and Matsuyama, T. 1979. Edge preserving smoothing, computer graphics and image processing. *Computer Graphics and Image Processing*, 9(4):394–407.
- Osher, S., Sole, A., and Vese, L. 2003. Image decomposition and restoration using total variation minimization and the H^{-1} norm. *Multiscale Modeling and Simulation: A SIAM Interdisciplinary Journal*, 1:(3)349–370.
- Ring, W. 2000. Structural properties of solutions to total variation regularization problems. *M2AN Mathematical Modeling and Numerical Analyses*. 34(4):799–810.
- Rudin, L.I., Osher, S., and Fatemi, E. 1992. Nonlinear total variation based noise removal algorithms *Physica D*, 60:259–268.

- Scherzer, O. 1998. Denoising with higher order derivatives of bounded variation and an application to parameter estimation. *Computing*, 60:1–27.
- Terzopoulos, D. 1986. Regularization of inverse visual problems involving discontinuities. *IEEE Transactions on Pattern Analysis and Machine Intelligence*, 8(4):413–424.
- Terzopoulos, D. 1988. The computation of visible-surface representations. *IEEE Trans Pattern Anal Mach Intell*, 10(4):417–438.
- Weickert, J. 1998. *Anisotropic Diffusion in Image Processing*, Stuttgart, B.G. Teubner.
- You, Y-L. and Kaveh, M. 2000. Fourth-order partial differential equation for noise removal. *IEEE Transactions on Image Processing*, 9(10):1723–1730.
- Ziemer, W. P. 1989. *Weakly Differentiable Functions, vol. 120 of Graduate Texts in Mathematics*. Springer-Verlag, New York, Sobolev spaces and functions of bounded variation.